

Phase behaviour and dynamics in primitive models of molecular ionic liquids

G.C. Ganzenmüller^{1*}, P.J. Camp^{2†}

¹ Fraunhofer Ernst Mach Institute for High-Speed Dynamics, 4 Eckerstrasse, 79104 Freiburg, Germany

² School of Chemistry, The University of Edinburgh, West Mains Road, Edinburgh EH9 3JJ, United Kingdom

Received March 4, 2011

The phase behaviour and dynamics of molecular ionic liquids are studied using primitive models and extensive computer simulations. The models account for size disparity between cation and anion, charge location on the cation, and cation-shape anisotropy, which are all prominent features of important materials such as room-temperature ionic liquids. The vapour-liquid phase diagrams are determined using high-precision Monte Carlo simulations, setting the scene for in-depth studies of ion dynamics in the liquid state. Molecular dynamics simulations are used to explore the structure, single-particle translational and rotational autocorrelation functions, cation orientational autocorrelations, self diffusion, viscosity, and frequency-dependent conductivity. The results reveal some of the molecular-scale mechanisms for charge transport, involving molecular translation, rotation, and association.

Key words: ionic liquids, vapour-liquid transition, dynamics, computer simulation

PACS: 61.20.Ja, 64.70.F-, 66.10.C-, 66.10.Ed, 66.20.-d

1. Introduction

Molecular ionic liquids are low-melting point compounds made up of molecular cations and anions. Currently, the most important examples are room-temperature ionic liquids (RTILs), which have very low vapour pressures, solvate a wide range of polar and non-polar solutes, and have been shown to catalyse chemical transformations when used as reaction media [1]. Typical cations (such as dialkylimidazolium) may exhibit both ionic and non-ionic characteristics. For instance, solutions of RTILs and water lead to the formation of micellar phases [2–6]. In terms of transport properties, RTILs are generally considered quite viscous and the diffusion constants are correspondingly low as compared to those in non-ionic molecular liquids. Experimentally, measurements of the frequency-dependent dielectric response yield insights on microscopic motions that lead to a change of polarization and, through the fundamental link between dielectric response and conductivity [7, 8], to the transport of charge. The dielectric spectra of many common RTILs have been measured [9–14]. Of particular note, Weingärtner and colleagues found evidence for a contribution to the dielectric spectra of 1-alkyl-3-methylimidazolium salts likely arising from cation rotations [15–17]. An analysis of dielectric spectra and nuclear-magnetic relaxation measurements highlighted motions on the order of tens of picoseconds (corresponding to real frequencies $\nu \sim 10^{11}$ Hz). Computer-simulation results have been used to resolve the different contributions to the dielectric spectrum, with the conclusion that the dielectric relaxation arising from molecular translations is faster than that from molecular rotations [15].

Atomistic simulations have yielded invaluable insights on the important molecular interactions and correlations in specific systems [18, 19]; there are far too many simulation studies to mention here, but a review by Maginn highlights the main achievements and outstanding challenges [20]. Low-frequency dynamics can be studied in atomistic simulations [21] but with some difficulty. The primary problem is that to calculate transport coefficients or frequency-dependent response

*E-mail: georg.ganzenmueller@emi.fraunhofer.de

†E-mail: philip.camp@ed.ac.uk

functions requires accurate calculations of appropriate time-correlation functions, but the rate of decay of these functions is characteristically long in RTILs and it is a challenge to calculate the long-time tails with acceptable signal-to-noise ratios [20]. Free-energy calculations and the construction of phase diagrams are other areas where the complexity of atomistic models may push the calculations out of reach. Therefore, to achieve a more comprehensive survey of dynamics over broad timescales – as well as the structure and phase behaviour – one might consider simplified models in which certain molecular characteristics can be tuned at will.

Clearly, the main molecular characteristics of RTILs are that the ions are of different sizes, the charges are distributed unevenly over the ions (especially in typical cations), and the cations are normally far from spherical. Typical anions such as Cl^- , BF_4^- , or PF_6^- , may be considered spherical in a first approximation, but cations such as dialkylimidazolium or dialkylpiperidinium are heterocyclic species. In the same way that a fluid of charged hard spheres, the restricted primitive model (RPM), serves as a basic model of simple molten salts, certain extensions to allow for the aforementioned molecular characteristics can be studied to gain insight on molecular ionic liquids. Malvaldi and Chiappe studied the dynamics in primitive models of RTILs consisting of dumbbell cations (each made up of two soft spheres, with one or both carrying a central charge) and simple soft-sphere anions [22]. It was shown that, even with such a simple model, certain experimental observations could be reproduced and rationalised in microscopic terms. For instance, in some imidazolium RTILs, the diffusion constant of the cation is greater than that of the anion [23, 24]; atomistic simulations show that the cation diffuses preferentially by moving in the direction of the carbon in the 2 position on the five-membered ring (in between the nitrogens at the 1 and 3 positions) [25]. This translational anisotropy is captured to some degree by Malvaldi and Chiappe's dumbbell model where the charge is distributed equally between the two halves; at low temperature and high density, the cation diffuses faster than the anion. Spohr and Patey have performed a highly systematic and comprehensive survey of the microscopic structure and dynamics in models consisting of a large spherical cation carrying a point charge displaced from the centre, and a simple soft-sphere anion. By controlling the location of the cation charge and cation-anion size disparity, a number of experimental trends could be rationalised on the basis of ion-ion correlations [26–28]. Specifically, many of the experimentally observed dependences of shear viscosity, conductivity, and diffusion constants on relative ion size, molecular charge distribution, and temperature could be mimicked with the simple models. Recent work on such models has even captured the effects of a polar solvent/impurity, such as water [29].

Regarding phase behaviour, the available thermodynamic data on RTILs show some interesting trends. For instance, the vapour-liquid critical temperature (T_c) – although difficult to measure directly in experiments because of molecular decomposition at high temperatures – appears to decrease with increasing molecular weight of the alkyl chains on the imidazolium cations, despite the growing van der Waals interactions favouring an increase in T_c [30]. Martín-Betancourt et al. constructed coarse-grained models in which the cations are represented by charged hard spherocylinders, and performed high-precision Monte Carlo (MC) simulations to determine the coexistence envelopes and critical points [31]. The critical temperature and density both decrease with increasing cation elongation, in qualitative correspondence with experimental data, due to the growing entropic role played by the steric bulk of the cation. Schröer and Vale surveyed fluid-fluid phase separations in solutions of imidazolium salts in a variety of polar and non-polar solvents, and showed that the phase diagrams could be analysed in terms of those for charged hard spheres with size asymmetry [32]. The main conclusion here was that the phase separation is mainly driven by Coulombic interactions, and that steric and dispersion interactions (which can be controlled systematically with substituents on the cations) modify the critical parameters. Models such as size-asymmetric charged hard spheres can be studied to yield systematic variations in critical parameters with cation size; integral-equation studies point to some non-trivial effects [33, 34].

In this work, primitive models of molecular ionic liquids are constructed and their phase behaviour and dynamical properties are examined. The models are chosen to reflect some of the key molecular characteristics, such as a size disparity between cation and anion, the location of the positive charge on the molecular cation, and the shape anisotropy of the cation. By constructing simple models possessing each of these characteristics, the essential relationships between molecu-

lar properties and dynamical behaviour can be identified. First, the vapour-liquid phase diagrams are computed using high-precision MC simulations. Then, molecular dynamics (MD) simulations of the dense liquid are performed in order to evaluate the microscopic structure and the transport coefficients – diffusion constants, viscosity, and conductivity. The dependences of these properties on molecular architecture and temperature are briefly discussed. Finally, the frequency-dependent conductivity is considered and the contributions from cation translations and rotations are resolved by comparing the conductivity spectrum with the spectra of the translational and rotational-velocity autocorrelation functions; the orientational correlations of the cations are also considered. The possible relevance of these results to experimental measurements of the dielectric response is discussed.

This paper is organised as follows. In section 2, the molecular models and parameters are defined. Monte Carlo simulations of phase behaviour are presented in section 3, focusing on the vapour-liquid coexistence envelope and the associated critical point. Molecular dynamics simulations of microscopic structure and (frequency-dependent) transport properties are discussed in section 4. Section 5 concludes the paper.

2. Models

The primitive models are presented in figure 1. In each case the anion is modelled as a single charged Lennard-Jones (LJ) sphere with energy parameter ϵ , diameter σ , charge $-q$, and mass $2m$. In the symmetric dumbbell (SD) and asymmetric dumbbell (AD) models, each cation is modelled with two LJ spheres (with LJ parameters ϵ and σ , and mass m) fused together at a distance $d = \sigma/\sqrt{2}$: in the SD model, each sphere carries a central charge of $+q/2$; in the AD model, only one sphere carries a central charge $+q$. In the corresponding symmetric-sphere (SS) and asymmetric-sphere (AS) models, each cation is formed from a single large LJ sphere with diameter σ_+ , energy parameter ϵ , and mass $2m$. The diameter σ_+ is chosen so that the excluded volume $4\pi\sigma_+^3/3$ is equal to that of the dumbbells defined above. The excluded volume of two dumbbells with sphere diameter σ and separation d is given approximately by [35]

$$\frac{\pi\sigma^3}{6} \left[8 + 12 \left(\frac{d}{\sigma} \right) + 3 \left(\frac{d}{\sigma} \right)^2 - \left(\frac{d}{\sigma} \right)^3 \right]. \quad (2.1)$$

With $d = \sigma/\sqrt{2}$, the effective cation diameter is $\sigma_+ \simeq 1.3014\sigma$. The charges on the cations are placed so that the shortest distance to the edge is always $\sigma/2$: in the SS model, two charges $+q/2$

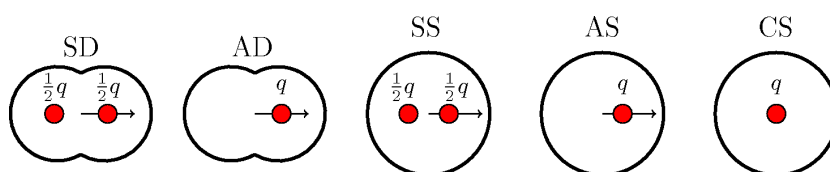


Figure 1. Models of primitive liquids distinguished by the model for the cation: symmetric dumbbell (SD); asymmetric dumbbell (AD); symmetric sphere (SS); asymmetric sphere (AS); centred sphere (CS). In each case, the anion is modelled as a single charged LJ sphere with diameter σ , charge $-q$, and mass $2m$. The SD and AD cations are each modelled with two LJ spheres of diameter σ and mass m , fused together at a distance $d = \sigma/\sqrt{2}$: in the SD model, each sphere carries a charge $+q/2$; and in the AD model, only one sphere carries the charge $+q$. The SS, AS, and CS cations are each modelled by a charged LJ sphere with diameter $\sigma_+ = 1.3014\sigma$ and mass $2m$: the SS cation carries two charges $+q/2$ displaced symmetrically from the centre by 0.1507σ ; the AS cation has a single charge $+q$ located 0.1507σ from the centre; the CS cation has its charge $+q$ at the centre. With these choices, the mass of each cation is $2m$, the shortest distance from the positive charge(s) to the edge is $\sigma/2$ (except for the CS model), and the excluded volume of each cation is the same. For the SD, AD, SS, and AS models, arrows indicate the unit vectors used to define the orientational autocorrelation function in section 4.3.

are displaced symmetrically from the centre by a distance $(\sigma_+ - \sigma)/2 = 0.1507\sigma$; in the AS model, one charge $+q$ is placed 0.1507σ from the centre. Finally, in the centred-sphere (CS) model, the cation consists of a single charged LJ sphere with diameter $\sigma_+ = 1.3014\sigma$, energy parameter ϵ , mass $2m$, and central charge $+q$. With this set of parameters, the excluded volumes for all cations are equal, the shortest distances from the charges to the edges are all equal to $\sigma/2$ (except for the CS model), the charges on the cations and anions are $\pm q$, and the cations and anions have equal masses of $2m$. The interactions between ions are given by a sum of LJ and Coulombic (C) site-site interactions. The LJ interaction between two spheres i and j is given by

$$u_{ij}^{\text{LJ}} = 4\epsilon \left[\left(\frac{\sigma_{ij}}{r_{ij}} \right)^{12} - \left(\frac{\sigma_{ij}}{r_{ij}} \right)^6 \right], \quad (2.2)$$

where $\sigma_{ij} = (\sigma_i + \sigma_j)/2$, r_{ij} is the centre-centre distance between spheres, and for simplicity the energy parameter ϵ is the same for all interactions. The charge-charge interaction is

$$u_{ij}^{\text{C}} = \frac{q_i q_j}{\mathcal{E} s_{ij}}, \quad (2.3)$$

where q_i is the charge on particle i , s_{ij} is the distance between charges i and j , and $\mathcal{E} = 4\pi\epsilon_0$ in which ϵ_0 is the dielectric permittivity of the vacuum. The reduced charge is defined as $q^* = \sqrt{q^2/\mathcal{E}\sigma\epsilon}$; in this work, there is given a fixed value of $q^* = 7$. This is appropriate for monovalent ions ($q = e$) and realistic choices for the LJ energy parameter $\epsilon/k_{\text{B}} \simeq 600$ K and the LJ diameter $\sigma \simeq 5$ Å. For each of the dumbbell models, the reduced moment of inertia of the cation is $I^* = I/m\sigma^2 = 0.25$; the same value is used for each of the spherical-cation models. Other reduced units are defined using ϵ , σ , and m : the reduced temperature is $T^* = k_{\text{B}}T/\epsilon$, where k_{B} is Boltzmann's constant; the reduced ion-pair concentration $\rho^* = N\sigma^3/V$, where N is the number of ion pairs and V is the volume; the reduced pressure $P^* = P\sigma^3/\epsilon$; and the reduced time $t^* = t/\tau$ where $\tau = \sqrt{m\sigma^2/\epsilon}$. With the typical values of ϵ and σ given above, along with a characteristic salt molecular weight of $4m \simeq 300$ g mol⁻¹, the basic unit of time is $\tau \simeq 1.94$ ps.

The phase diagrams of the model systems were determined using MC simulations; the simulation method and results are presented in section 3. Subsequently, the dynamical properties were determined using MD simulations; the computational details and results are presented in section 4. In all cases, the systems were simulated in cubic boxes of side L and with periodic boundary conditions applied. The LJ interactions were truncated and shifted at $L/2$, and the Coulombic interactions were handled using the Ewald summation with conducting periodic boundary conditions [36].

3. Phase behaviour

3.1. Monte Carlo simulations

To identify the liquid region of the phase diagram and to focus the subsequent dynamical studies, vapour-liquid coexistence envelopes were determined using a MC technique. Wang-Landau simulations were performed in the grand-canonical ensemble according to the GCMCWL scheme described in reference [37]. Essentially, this is a flat-histogram sampling method that enables an iterative determination of the canonical partition function $Q(N, V, T)$ as a function of N at fixed V and T . The conditions for phase coexistence are then easily determined using an equal-area criterion applied to the bimodal particle-number distribution $p(N) \propto z^N Q(N, V, T)$, where z is the activity. Full details are given in reference [37]. The current simulations were carried out in cubic boxes with sides $L = 11.75\sigma$ and $L = 13\sigma$ for dumbbell and sphere models, respectively. The GCMCWL technique has been successfully applied to a number of 'tough' systems where a large degree of clustering is anticipated near the coexistence region, including charged soft spheres [37] and dipolar spheres [38].

3.2. Vapour-liquid coexistence envelopes

Vapour-liquid coexistence envelopes for the SD, AD, and AS systems are shown in figure 2. In order to assess the effects of the Coulombic interactions, results are also shown for an equimolar mixture of *uncharged* dumbbells and LJ spheres (the SD/AD model with $q = 0$). The critical parameters were estimated by fitting the simple scaling law

$$\rho_{\pm} = \rho_c + At \pm Bt^{\beta} \quad (3.1)$$

to near-critical coexistence densities in the vapour (ρ_-) and liquid (ρ_+) phases, where ρ_c is the critical density, $t = 1 - T/T_c$, and $\beta = 0.3265$ is the 3D Ising order-parameter exponent. Ionic criticality is known to be Ising-like [39]. The fitted scaling laws are shown in figure 2.

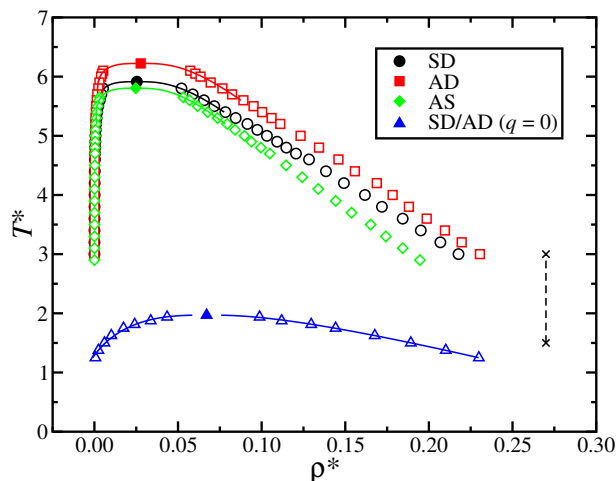


Figure 2. (Color on-line) Phase diagrams of selected primitive models of ionic fluids: (circles) SD model; (squares) AD model; (diamonds) AS model; (triangles) SD/AD model with $q = 0$. Open symbols indicate sub-critical coexistence points, filled symbols indicate the critical points, and the lines show the fits from the scaling law in equation (3.1). The dashed line indicates the temperature range along the $\rho^* = 0.27$ isochore studied using molecular dynamics simulations.

The critical parameters are given in table 1. By comparing the charged and uncharged cases, it is clear that the Coulombic interactions result in a large increase in the critical temperature and a substantial decrease in the critical density. A low critical density is one characteristic of an ionic critical point [40], and with the current parameters, the Coulombic interactions are very strong. To compare the current results with those for the simple case of charged hard spheres – the restricted primitive model (RPM) – table 1 also shows the packing fraction η at the critical point. For the systems studied here, the volumes of the ions are estimated by approximating them as hard particles. For the SD and AD models, the volume of a dumbbell is

$$v(d) = \frac{\pi\sigma^3}{6} \left[1 + \frac{3}{2} \left(\frac{d}{\sigma} \right) - \frac{1}{2} \left(\frac{d}{\sigma} \right)^3 \right]. \quad (3.2)$$

The key point is that $\eta_c \simeq 0.04$ for all charged models, including the RPM. The comparison of critical temperatures is not that straightforward. The RPM critical temperature is $k_B T_c = 0.05069(2)q^2/\mathcal{E}\sigma$ [39], where $-q^2/\mathcal{E}\sigma$ is the Coulombic interaction between a cation and an anion at contact. For the primitive models studied here, the minimum in the interaction potential between two oppositely charged LJ spheres is $r_{\min} \simeq 0.9556\sigma$ and $u_{\min} = -49.63\epsilon$. The reduced critical temperatures are all in the region of $T_c^* = 6$ and so the corresponding ‘ionic’ temperature is $k_B T_c/|u_{\min}| \simeq 0.12$. This is considerably higher than the RPM value, reflecting the soft cores of the particles and the additional LJ attractions. Model AD has the highest critical temperature, reflecting the fact that there are a large number of cation-anion arrangements where the charge

Table 1. Vapour-liquid critical parameters for selected primitive models of ionic fluids (including the RPM [39]) and for an uncharged system of dumbbells and LJ spheres (SD/AD model with $q = 0$). $T_c^* = k_B T_c / \epsilon$ is the reduced critical temperature, $\rho_c^* = \rho_c \sigma^3$ is the reduced critical ion-pair density, and η_c is the critical packing fraction calculated from ρ_c^* assuming hard particles of dimension σ . The figures in brackets are the estimated uncertainties in the final digits.

Model	T_c^*	ρ_c^*	η_c
SD	5.91(2)	0.0255(1)	0.0385(3)
AD	6.22(2)	0.0281(2)	0.0424(3)
AS	5.80(2)	0.0247(1)	0.0414(2)
SD/AD ($q = 0$)	1.970(8)	0.0671(6)	0.1013(9)
RPM [39]	0.05069(2) q^{*2}	0.0395(1)	0.0414(1)

separation is about 1σ and the Coulombic interaction is strong. The number of such arrangements is reduced when the cation charge is split between two centres, as in the SD model, because now the anion has to be in the right place to satisfy two site-site interactions. For model AS, only one arrangement of the anion and cation gives a charge-charge separation of about 1σ , and so the critical temperature is relatively low.

Knowledge of the vapour-liquid coexistence region facilitates the choice of the temperature and density for MD simulations in the liquid phase. The aim is to reach low temperatures (and hence low vapour pressures) while at the same time staying within the liquid region of the phase diagram. The choice $\rho^* = 0.27$ gives access to the liquid region of the phase diagram. Moreover, for a typical molecular ionic liquid with $\sigma = 5 \text{ \AA}$ and ion mass $2m \simeq 150 \text{ g mol}^{-1}$, this density equates to a mass density of about 1 g cm^{-3} , which closely corresponds to experimental values. The temperature range $1.5 \leq T^* \leq 3.0$ will be considered, as the upper limit is well within the liquid region for all models, while the lower limit approaches the region of spinodal decomposition.

4. Liquid-phase structure and dynamics

4.1. Molecular dynamics simulations

MD simulations were performed using the LAMMPS package [41, 42]. Systems of $N = 125$ ion pairs were simulated in a cubic box with edge length $L = 7.736\sigma$ giving a reduced ion-pair density of $\rho^* = 0.27$, as advertised in section 3.2. The dynamical equations of motion were integrated using the velocity-Verlet scheme with a timestep of $\delta t^* = 0.0025$. Simulations were started from a CsCl lattice structure and equilibrated at the desired temperature using simple velocity rescaling over 10^5 timesteps. Production runs were then performed in the canonical (NVT) ensemble over 7.2×10^6 timesteps (equivalent to around 35 ns) with weak coupling to a Berendsen thermostat [36]. Ion positions and velocities, and all components of the stress tensor, were saved at intervals of 4

Table 2. Reduced pressure P^* along the isochore $\rho^* = 0.27$ as a function of temperature, for each of the charged models.

T^*	Model				
	SD	AD	SS	AS	CS
1.50	-1.76	-1.62	-1.78	-0.30	-1.52
1.75	-1.13	-1.36	0.16	0.41	0.08
2.00	-0.45	-0.75	1.17	1.10	1.17
2.25	0.22	-0.11	1.85	1.76	1.85
2.50	0.88	0.53	2.48	2.40	2.49
2.75	1.53	1.16	3.12	3.02	3.13
3.00	2.17	1.79	3.73	3.63	3.73

timesteps for post-processing. The production runs were divided into 12 blocks, and statistical uncertainties were estimated by assuming block averages to be statistically independent. Table 2 shows the values of the pressure along the isochore $\rho^* = 0.27$ for each of the charged models. At temperatures $T^* < 2.5$, the pressure in at least one of the systems is negative, indicating that these state points may well be mechanically unstable and/or within a binodal region. Figure 2 confirms that these low temperatures are approaching the vapour-liquid coexistence region.

4.2. Structure

The microscopic structure in the liquids was examined using the radial distribution functions (RDFs) $g_{\alpha\beta}(r)$ ($\alpha, \beta = +, -$) [43]. These functions are given by

$$g_{\alpha\beta}(r) = \frac{V}{4\pi N_\alpha N_\beta r^2} \left\langle \sum_i^{N_\alpha} \sum_{j \neq i}^{N_\beta} \delta(r - r_{ij}) \right\rangle, \quad (4.1)$$

where $N_+ = N_- = N$, and r_{ij} is the distance between the centres of mass of particles i and j . MD simulation results at $T^* = 2.5$ are shown in figure 3; this temperature was selected in order to be sure of simulating a single dense liquid phase. Firstly, the cation-cation RDF (g_{++}) and anion-anion

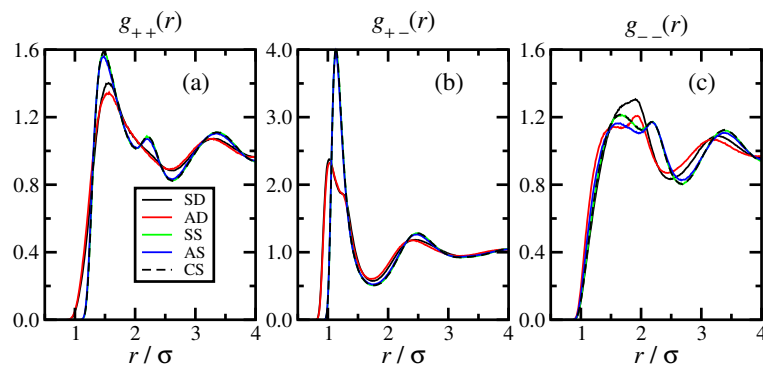


Figure 3. (Color on-line) Pair-correlation functions in the liquid phase at $\rho^* = 0.27$ and $T^* = 2.5$: (a) cation-cation RDF, $g_{++}(r)$; (b) cation-anion RDF, $g_{+-}(r)$; (c) anion-anion RDF, $g_{--}(r)$. In all cases, the separation r is that between centres of mass.

RDF (g_{--}) show primary peaks at around $r \simeq 1.5\sigma$ for all models. The cation-anion RDF (g_{+-}) shows strong correlations at much shorter distances, but there is a marked difference between the spherical models (SS, AS, CS) and the dumbbell models (SD, AD), reflecting the shapes of the cations. The spherical models show one primary peak at $r \simeq 1.1\sigma$, roughly equal to the distance of closest approach $(\sigma + \sigma_+)/2 \simeq 1.15\sigma$. The dumbbells models exhibit a short-range double-peaked feature: the peak near $r \simeq 1\sigma$ is clearly due to the anion sitting in the ‘valley’ between the two spheres of the cation dumbbell; the peak near $r \simeq 1.3\sigma$ roughly corresponds to the anion being located near the dumbbell axis, at a distance $\sigma + d/2 \simeq 1.21\sigma$ from the cation centre of mass. This picture is in good correspondence with work on similar models by Malvaldi and Chiappe [22].

4.3. Dynamics

A range of dynamical properties has been calculated. The frequency-dependent conductivity, $\kappa(\omega)$, is related to the charge current defined by

$$\mathbf{J}(t) = \sum_{i=1}^{N_q} q_i [\mathbf{v}_i^{\text{com}}(t) + \Delta \mathbf{v}_i(t)], \quad (4.2)$$

where the sum runs over all charge sites (of which there are N_q), $\Delta \mathbf{v}_i(t)$ is the velocity of charge i in its molecular centre-of-mass frame, and $\mathbf{v}_i^{\text{com}}(t)$ is the corresponding molecular centre-of-mass

velocity. (Obviously, $\Delta \mathbf{v} = 0$ for the anions.) The frequency-dependent conductivity is given by [43]

$$\kappa(\omega) = \kappa'(\omega) + i\kappa''(\omega) = \frac{1}{3Vk_{\text{B}}T} \int_0^{\infty} \langle \mathbf{J}(t) \cdot \mathbf{J}(0) \rangle \exp(-i\omega t) dt, \quad (4.3)$$

where $i = \sqrt{-1}$, and $\kappa'(\omega)$ and $\kappa''(\omega)$ are the real (in-phase) and imaginary (out-of-phase) parts, respectively. The static conductivity is $\kappa = \kappa(0)$. The contributions of different single-particle motions to the conductivity spectrum can be determined by calculating ion translational velocity autocorrelation functions $C_v(t)$ [43], and a cation intramolecular velocity autocorrelation function $C_{\Delta}(t)$:

$$C_v(t) = \langle \mathbf{v}_i^{\text{com}}(t) \cdot \mathbf{v}_i^{\text{com}}(0) \rangle, \quad (4.4)$$

$$C_{\Delta}(t) = \langle \Delta \mathbf{v}_i(t) \cdot \Delta \mathbf{v}_i(0) \rangle. \quad (4.5)$$

These two functions capture the dynamics of the molecular centre of mass [$C_v(t)$] and the intramolecular rotations [$C_{\Delta}(t)$] [8]. The ion diffusion constants are obtained from the standard Green-Kubo relationship

$$D = \frac{1}{3} \int_0^{\infty} C_v(t) dt. \quad (4.6)$$

The reorientational dynamics of the cations are examined by calculating the correlation function

$$C_e(t) = \langle \mathbf{e}_i(t) \cdot \mathbf{e}_i(0) \rangle, \quad (4.7)$$

where $\mathbf{e}(t)$ is the orientation unit vector along the cylindrical symmetry axis of the cation. An associated correlation time can be defined by

$$\tau_e = \int_0^{\infty} C_e(t) dt. \quad (4.8)$$

Finally, the viscosity of the fluid is calculated using the Green-Kubo formula involving the auto-correlation function of the off-diagonal elements of the stress tensor $\Pi_{xy}(t)$:

$$\eta = \frac{1}{Vk_{\text{B}}T} \int_0^{\infty} \langle \Pi_{xy}(t) \Pi_{xy}(0) \rangle dt. \quad (4.9)$$

The static transport properties are considered first, namely the diffusion constants (D), shear viscosity (η), and static conductivity (κ). In reduced units, these properties are defined by $D^* = D\tau/\sigma^2$, $\eta^* = \eta\sigma^3/\epsilon\tau$, and $\kappa^* = \kappa\tau/\mathcal{E}$. These properties were measured for each charged model as functions of temperature. In accord with Eyring's activated-dynamics picture [44], it turns out that the data are fitted adequately with Arrhenius relations of the form

$$D \propto \exp(-E_a/k_{\text{B}}T), \quad \eta \propto \exp(E_a/k_{\text{B}}T), \quad \kappa \propto \exp(-E_a/k_{\text{B}}T), \quad (4.10)$$

where E_a is an activation energy associated with that particular transport property. The logarithms of the transport properties are plotted as functions of $1/T^*$ in figure 4, along with Arrhenius-law fits. Simulations at $T^* = 1.5$ gave erratic and anomalous results, probably due to the system being within either the liquid-solid or vapour-liquid coexistence region; these data points are omitted from the plots. Arrhenius-like behaviour is observed over the temperature range considered. In general, for a given temperature, the cation and anion diffusion constants obey $D_+ < D_-$ due to the larger steric bulk of the cations. The dumbbells models (SD and AD) exhibit higher values of D_+ than the sphere models (SS, AS, CS). This may be attributed to the elongated shape of the dumbbell cations, facilitating the motion along their long axes. For the dumbbell cations, a symmetric charge

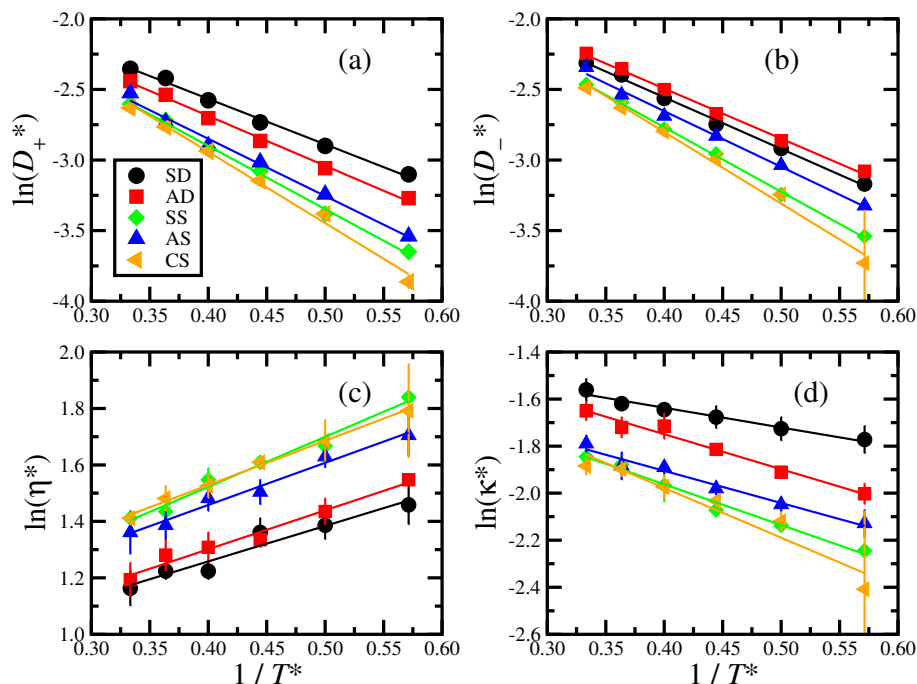


Figure 4. (Color on-line) Arrhenius plots of transport properties at $\rho^* = 0.27$ and $1.75 \leq T^* \leq 3.00$: (a) cation diffusion constant D_+ ; (b) anion diffusion constant D_- ; (c) shear viscosity η ; (d) static conductivity κ . Results are plotted in reduced units defined in the text.

distribution gives a higher value of D_+ than an asymmetric charge distribution, which probably arises from there being less strong interactions (on average) between an SD cation, and its nearest-neighbour anions. For the spherical cations, the reverse is true, although the magnitude of the effect is smaller. In general, D_- mirrors the trends seen in D_+ , indicating strong association between oppositely charged ions. Using the molecular parameters given in section 2, the reduced values $D^* \simeq 0.03$ – 0.10 correspond to real values $D \simeq 0.3$ – $1.0 \times 10^{-7} \text{ m}^2 \text{ s}^{-1}$, which are a little higher than typical results for RTILs. The shear viscosity η shows the reverse trend to D_{\pm} , with the dumbbells models being least viscous; this can be rationalised qualitatively on the basis of a Stokes-Einstein relationship of the form $D \propto 1/\eta$ [43]. The reduced values $\eta^* \simeq 3$ – 5 equate to real values of $\eta \simeq 3$ – $5 \times 10^{-4} \text{ Pa s}$. These are much smaller than the viscosities of real RTILs, which are normally on the scale of tens of mPa s. The trends in the static conductivity mirror those in D_{\pm} , which can be rationalised with a generalised Nernst-Einstein relationship of the form [43]

$$\kappa = \frac{\rho q^2}{k_B T} (D_+ + D_-) (1 - \Delta), \quad (4.11)$$

where Δ characterises the deviation from pure Nernst-Einstein behaviour, which is observed when there are no cross correlations between cation and anion motions. Such correlations lead to a reduction in κ and hence $\Delta > 0$. For the data shown in figure 4, $\Delta \simeq 0.75$, a large value that arises from very strong cation-anion correlations. The reduced values $\kappa^* \simeq 0.1$ – 0.2 correspond to real values of $\kappa \simeq 6$ – 12 S m^{-1} , which are somewhat higher than those seen in experiments on RTILs. In summary, then, for dumbbell cations, a symmetric charge distribution gives higher diffusion constants, lower shear viscosity, and higher static conductivity. The dependences of transport properties with spherical cations are less sensitive to the charge distribution.

The activation energies associated with the static transport properties are reported in table 3. In general, the dumbbell-cation models exhibit lower activation energies. This correlates with the picture presented above, with the elongated models being more capable of breaking out of transient molecular cages by moving along their long axes. When converted to real energy units – using the

Table 3. Activation energies obtained from Arrhenius-law fits to the temperature dependence of the cation diffusion constant (D_+), the anion diffusion constant (D_-), the shear viscosity (η), the static conductivity (κ), and an orientational correlation time (τ_e). Figures in brackets are estimated uncertainties in the final digits.

Model	Activation energies E_a/ϵ				
	D_+	D_-	η	κ	τ_e
SD	3.28(13)	3.71(13)	1.27(21)	0.823(80)	2.452(43)
AD	3.63(12)	3.636(96)	1.47(10)	1.532(93)	2.938(51)
SS	4.51(14)	4.580(89)	1.806(73)	1.70(14)	1.301(39)
AS	3.98(26)	4.10(25)	1.55(14)	1.47(11)	1.748(37)
CS	4.79(18)	4.546(38)	1.725(62)	1.51(12)	

molecular parameters given in section 2 – the activation energies for diffusion are in the region of 20 kJ mol^{-1} , which is a typical value for some RTILs [13]. The activation energies for viscosity and conductivity are in the region of $5\text{--}10 \text{ kJ mol}^{-1}$, which are the right order of magnitude but a little too low. Experimental results for RTILs show significant deviations from Arrhenius behaviour and are usually fitted with a Vogel-Fulcher-Tammann equation of the form $A \exp[B/(T - T_0)]$, so these are not directly comparable to the Arrhenius-law fits presented here. Nonetheless, B/k_B is typically of order $500\text{--}1000 \text{ K}$, which in the current reduced units equates to around $B/\epsilon \simeq 1\text{--}2$; this is at least the same order of magnitude as the activation energies presented in table 3.

The dynamics are now considered in more detail for a single state point, $\rho^* = 0.27$ and $T^* = 2.5$. This temperature is chosen such that each of the models is in its liquid phase, away from the coexistence region. Figure 5 shows the conductivity spectra $\kappa(\omega)$ for all five models. The spectra of the SD and AD models are characterised by broad shoulders in the real parts, $\kappa'(\omega)$, at frequencies $\omega^* \simeq 10\text{--}20$, and single peaks in the imaginary parts, $\kappa''(\omega)$, at a frequency $\omega^* \simeq 30$. The spectrum for the CS model is particularly simple, with the real part exhibiting a peak that is characteristic of ionic liquids [45–47]. The low-frequency, negative portion of the imaginary part signals that ion translations may contribute to the low-frequency complex dielectric spectrum

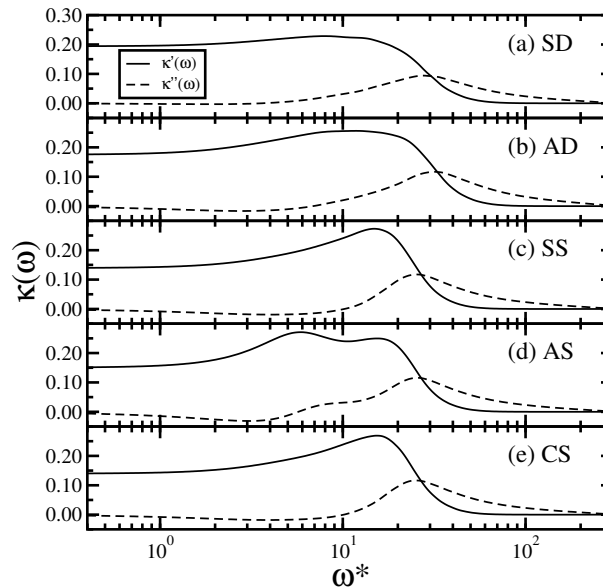


Figure 5. Real and imaginary parts of the conductivity spectrum, $\kappa'(\omega)$ (solid lines) and $\kappa''(\omega)$ (dashed lines), respectively, for primitive models at $\rho^* = 0.27$ and $T^* = 2.5$: (a) SD model; (b) AD model; (c) SS model; (d) AS model; (e) CS model.

$\varepsilon(\omega) = 1 + 4\pi i\kappa(\omega)/\omega$ [21]. The spectrum of the SS model looks very similar to that of the CS model, showing that a symmetrical displacement of charge on the cation does not strongly affect the conductivity. This is natural, because these two models share the same centre of mass and the same centre of charge; the displacement of charge should only affect the degree of interactions between cations and anions, and is not expected to lead to new qualitative features in $\kappa(\omega)$. Very interesting features arise in the spectrum of the AS model. Here, the real part contains two, very-well resolved peaks at reduced frequencies of around $\omega^* = 5$ and $\omega^* = 20$.

To help identify the molecular motions responsible for the features in $\kappa(\omega)$, figure 6 shows the real part along with the spectra of $C_v(t)$ (for each of the ions) and that of $C_\Delta(t)$:

$$C(\omega) = 2 \int_0^\infty C(t) \cos(\omega t) dt. \quad (4.12)$$

Recall that $C_v(t)$ describes the centre-of-mass motions of the ions, while intramolecular rotations of the cations are described by $C_\Delta(t)$. The spectra are basically densities of states for vibrations and librations within the solvation shell. Of course, these are single-particle properties, and in the following discussion, the cross-correlations between cations and anions (that lead to deviations from the Nernst-Einstein law) are ignored. Nonetheless, the single-particle properties will yield some insight on the collective dynamics that lead to the conductivity spectrum. For the purposes of comparison, each spectrum is normalised to unit area. For the SD and AD models, the cation translations, anion translations, and cation rotations occur on similar timescales. As a result, $\kappa'(\omega)$ exhibits a broad peak over the relevant range of frequencies. For the SS and AS models, the rotational spectra are much less broad than those for the SD and AD models. For the AS model, the peak in the rotational spectrum coincides with the low-frequency peak in $\kappa'(\omega)$, indicating that this feature of the conductivity arises from cation rotations. Of course, this feature is absent from $\kappa'(\omega)$ for the SS model, because the rotation of a symmetrical distribution of positive ions leads to no net transport of charge.

The peaks in the rotational spectra in figure 6 show that the spherical cations (SS and AS)

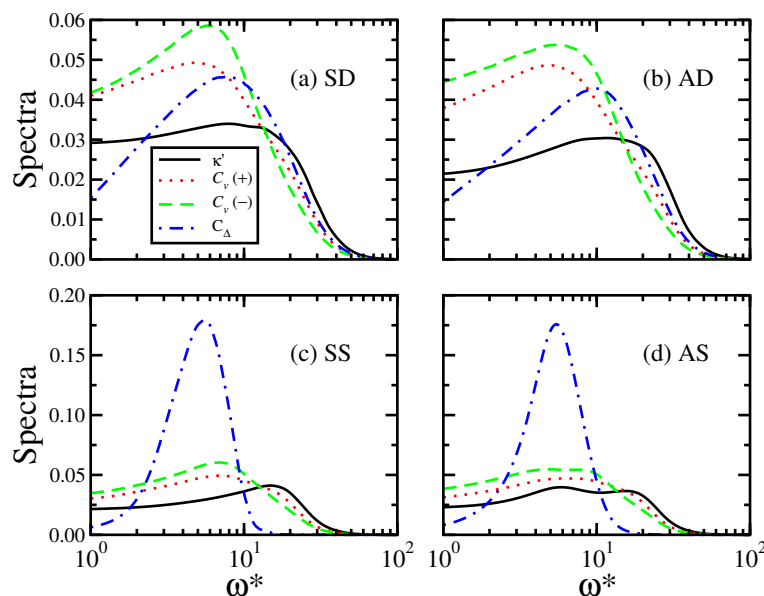


Figure 6. (Color on-line) Real part of the conductivity spectrum [$\kappa'(\omega)$] compared with the spectra of the centre-of-mass velocity autocorrelation functions for the cations and anions [$C_v(\omega)$], and the rotational velocity autocorrelation function for the cations [$C_\Delta(\omega)$], for primitive models at $\rho^* = 0.27$ and $T^* = 2.5$: (a) SD model; (b) AD model; (c) SS model; (d) AS model. In each case, the plots are normalised so that the frequency integral for each spectrum is equal to unity.

librate slower than the dumbbell cations, despite their having the same excluded volumes and equal moments of inertia. This difference is attributed to the so-called charge arm, described by Kobrak and Sandalow [48]. If a single charge q is displaced by a distance l_q from the cation centre of mass, then the librational frequency of rotation is proportional to l_q/I [48]; l_q is called the charge arm. Recall that in the present models, the charges are set a certain distance from the edge of the cations, and so they may be at different distances from the centres of mass. For the dumbbell models $l_q = \sigma/2\sqrt{2} \simeq 0.3536\sigma$, while for the spherical models $l_q = 0.1507\sigma$. Keeping the moment inertia $I^* = 0.25$ for the AD model and equating the ratio l_q/I for the AD and AS models gives $I^* = 0.1066$ for the AS model. Conductivity spectra and the spectra of the velocity autocorrelation functions have been calculated for the SS and AS models with $I^* = 0.1066$ (data not shown) and the rotational peak does indeed shift to higher frequency, coinciding with the peak frequencies for the SD and AD models. Correspondingly, the low-frequency peak in $\kappa'(\omega)$ shifts up in frequency and merges with the centre-of-mass peak.

The single-particle motions detailed here occur in the region of $\omega^* \simeq 5\text{--}20$, which equate to real frequencies $\nu \simeq 0.4\text{--}1.6$ THz. These are quite close to the natural timescales in RTILs: cation rotations in 1-alkyl-3-methylimidazolium salts occur on the timescale of tens of picoseconds [15–17]. Shim and Kim present $\kappa(\omega)$ from computer simulations of 1-ethyl-3-methylimidazolium hexafluorophosphate that exhibits a main peak at around 15 THz and a low-frequency shoulder below about 10 THz [21]; it is tempting to speculate that the low-frequency feature arises from cation rotations.

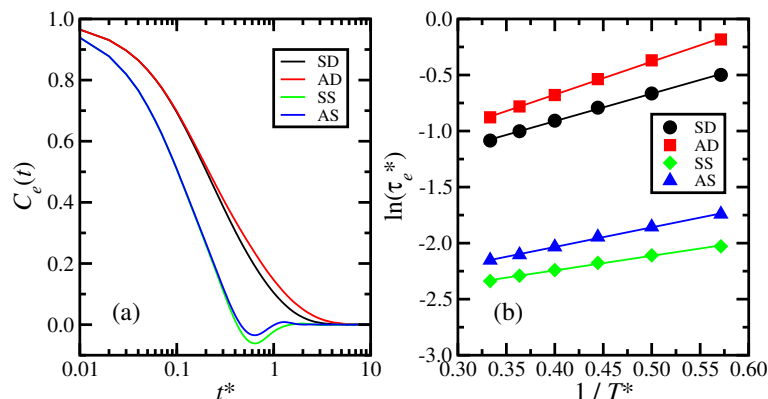


Figure 7. (Color on-line) (a) Orientational autocorrelation function $C_e(t)$ for primitive models at $\rho^* = 0.27$ and $T^* = 2.5$. (b) Arrhenius plot of the corresponding decay times τ_e for $1.75 \leq T^* \leq 3.00$. Results are plotted in reduced units defined in the text.

To explore cation reorientations further, figure 7 (a) shows $C_e(t)$ for the dumbbell-cation and spherical-cation models, at $\rho^* = 0.27$ and $T^* = 2.5$. Firstly, the dumbbell models exhibit a monotonous decay in $C_e(t)$, while the spherical models show a negative portion. The spherical models may undergo a rapid reversal in orientation on the timescale of $t \simeq 0.6\tau$ due to the absence of steric hindrance. Secondly, the correlations die away more slowly with dumbbells than with spheres, due to the packing effects that restrict the reorientation of the anisotropic dumbbells. Finally, an asymmetric charge distribution, as in the AD and AS models, leads to a slower decay of $C_e(t)$ as compared to the SD and SS models, respectively. This may be due to the anisotropy of the cation-anion interactions when a single, whole charge is localised near the edge of the cation, rather than being spread out over the molecule. To summarise, anisotropies in the short-range repulsions and electrostatic interactions lead to longer orientational correlation times. The decay time $\tau_e^* = \tau_e/\tau$ has been calculated as a function of temperature for each of the models; the results are presented on Arrhenius plots in figure 7 (b). The associated activation energies from the Arrhenius law $\tau_e \propto \exp(E_a/k_B T)$ are reported in table 3. The activation energies for the dumbbell models are greater than those for the spherical models, once again reflecting the steric barriers to rotation of dumbbells arising from their anisotropic shapes. An asymmetric charge distribution gives rise to

marginally higher barriers than does a symmetric one, reflecting the effect of anisotropy of cation-anion interactions. The decay times span the range $\tau_e^* \simeq 0.1\text{--}0.8$, which in real units correspond to the picosecond timescale; these are realistic values, at least for simple molecular liquids. When converted to real units, the activation energies are of order 10 kJ mol^{-1} , which as mentioned above, are at least of the right order of magnitude for molecular ionic liquids, but a bit too low.

5. Conclusions

Simple models of molecular ionic liquids were constructed in order to study the effects of ion-size disparity, cation-charge distribution, and cation-shape anisotropy. The cations were made up of charged soft spheres, with attractive interactions included: one type of cation consisted of a single sphere carrying either one charge at the centre or off-centre, or two charges displaced symmetrically from the centre; the other type of cation was a dumbbell, with either one or two of the constituent spheres carrying a charge. The anions were charged soft spheres. Such simple models admit in-depth studies of phase behaviour and dynamics in simulations of reasonable length, using normal computational facilities. The vapour-liquid coexistence curves were determined using Wang-Landau simulations and the resulting critical parameters were compared with those of the restricted primitive model, the simplest representation of an ionic fluid. The presence of attractive interactions increases the critical temperature above that expected from electrostatic interactions alone, while the critical density remains roughly constant and characteristically low.

Dynamics simulations were then conducted along a liquid-state isochore appropriate to typical ambient conditions. The microscopic structure has been studied using pair correlation functions, and rationalised in terms of the probable packing of the ions, and the resulting electrostatic interactions. The temperature dependences of the ion diffusion constants, shear viscosity, conductivity, and orientational correlation time are Arrhenius-like, at least over the temperature range considered here. The magnitudes of these properties, and the associated activation energies, when converted to real units, are not too dissimilar from those measured experimentally, although in general the diffusion constants and conductivity are too high, and the viscosity is too low. This is to be expected of such simple models with comparatively little ‘molecular roughness’. Coarse graining usually results in an effective decrease of molecular-scale friction, implying enhanced diffusion and conductivity, and reduced viscosity. This is a general drawback of coarse-grained models [49] which cannot always be remedied just by tuning the effective interactions; for instance, molecular-scale noise and friction can be restored with integration schemes similar to those used in dissipative particle dynamics simulations [50]. The variations in the transport coefficients between different models were rationalised in terms of microscopic correlations. The dynamics at a particular liquid-phase state point (high density, low temperature) were investigated in more detail by looking at the frequency-dependent conductivity, and the spectra of centre-of-mass and rotational velocity autocorrelation functions. For the models with dumbbell cations, the centre-of-mass and rotational motions occur on similar timescales, although only the centre-of-mass motions contribute to the conductivity spectrum if the positive charge is distributed symmetrically over the molecule. For the models with spherical cations and off-centre charges, the centre-of-mass and rotational motions occur on different timescales which, with an asymmetrical distribution of charge on the cation, lead to well-resolved features in the conductivity spectrum. The decay of orientational correlations was rationalised with reference to anisotropies of short-range repulsions and electrostatic interactions. Despite the simplicity of the models studied here, it is possible that some of the features observed in the detailed dynamics may also be observable in experimental studies of molecular ionic liquids.

Acknowledgements

The authors are privileged to contribute this work to the special issue of Condensed Matter Physics in honour of Professor Yura Kalyuzhnyi’s 60th birthday.

References

1. Welton T., *Chem. Rev.*, 1999, **99**, 2071; doi:10.1021/cr980032t.
2. Wang Y., Voth G.A., *J. Am. Chem. Soc.*, 2005, **127**, 12192; doi:10.1021/ja053796g.
3. Canongia Lopes J.N.A., Pádua A.A.H., *J. Phys. Chem. B*, 2006, **110**, 3330; doi:10.1021/jp056006y.
4. Canongia Lopes J.N., Costa Gomes M.F., Pádua A.A.H., *J. Phys. Chem. B*, 2006, **110**, 16816; doi:10.1021/jp063603r.
5. Triolo A., Russina O., Bleif H.J., Di Cola E., *J. Phys. Chem. B*, 2007, **111**, 4641; doi:10.1021/jp067705t.
6. Triolo A., Russina O., Fazio B., Appetecchi G.B., Carewska M., Passerini S., *J. Chem. Phys.*, 2009, **130**, 164521; doi:10.1063/1.3119977.
7. Schröder C., Haberler M., Steinhauser O., *J. Chem. Phys.*, 2008, **128**, 134501; doi:10.1063/1.2868752.
8. Schröder C., Steinhauser O., *J. Chem. Phys.*, 2009, **131**, 114504; doi:10.1063/1.3220069.
9. Schrödle S., Annat G., MacFarlane D.R., Forsyth M., Buchner R., Hefter G., *Chem. Commun.*, 2006, No. 16, 1748; doi:10.1039/B602209J.
10. Tokuda H., Hayamizu K., Ishii K., Susan M.A.B.H., Watanabe M., *J. Phys. Chem. B*, 2004, **108**, 16593; doi:10.1021/jp047480r.
11. Tokuda H., Hayamizu K., Ishii K., Susan M.A.B.H., Watanabe M., *J. Phys. Chem. B*, 2005, **109**, 6103; doi:10.1021/jp044626d.
12. Tokuda H., Ishii K., Susan M.A.B.H., Tsuzuki S., Hayamizu K., Watanabe M., *J. Phys. Chem. B*, 2006, **110**, 2833; doi:10.1021/jp053396f.
13. Hayamizu K., Tsuzuki S., Seki S., Fujii K., Suenaga M., Umebayashi Y., *J. Chem. Phys.*, 2010, **133**, 194505; doi:10.1063/1.3505307.
14. Mizoshiri M., Nagao T., Mizoguchi Y., Yao M., *J. Chem. Phys.*, 2010, **132**, 164510; doi:10.1063/1.3419906.
15. Schröder C., Wakai C., Weingärtner H., Steinhauser O., *J. Chem. Phys.*, 2007, **126**, 084511; doi:10.1063/1.2464057.
16. Wulf A., Ludwig R., Sasisanker P., Weingärtner H., *Chem. Phys. Lett.*, 2007, **439**, 323; doi:10.1016/j.cplett.2007.03.084.
17. Huang M.M., Bulut S., Krossing I., Weingärtner H., *J. Chem. Phys.*, 2010, **133**, 101101; doi:10.1063/1.3478221.
18. Del Pópolo M.G., Voth G.A., *J. Phys. Chem. B*, 2004, **108**, 1744; doi:10.1021/jp0364699.
19. Canongia Lopes J.N., Deschamps J., Pádua A.A.H., *J. Phys. Chem. B*, 2004, **108**, 2038; doi:10.1021/jp0362133.
20. Maginn E.J., *J. Phys.: Condens. Matter*, 2009, **21**, 373101; doi:10.1088/0953-8984/21/37/373101.
21. Shim Y., Kim H.J., *J. Phys. Chem. B*, 2008, **112**, 11028; doi:10.1021/jp802595r.
22. Malvaldi M., Chiappe C., *J. Phys.: Condens. Matter*, 2008, **20**, 035108; doi:10.1088/0953-8984/20/03/035108.
23. Umecky T., Kanakubo M., Ikushima Y., *Fluid Phase Equilib.*, 2005, **228–229**, 329; doi:10.1016/j.fluid.2004.08.006.
24. Kanakubo M., Harris K.R., Tsuchihashi N., Ibuki K., Ueno M., *J. Phys. Chem. B*, 2007, **111**, 2062; doi:10.1021/jp067328k.
25. Urahata S.M., Ribeiro M., *J. Chem. Phys.*, 2005, **122**, 024511; doi:10.1063/1.1826035.
26. Spohr H.V., Patey G.N., *J. Chem. Phys.*, 2008, **129**, 064517; doi:10.1063/1.2968544.
27. Spohr H.V., Patey G.N., *J. Chem. Phys.*, 2009, **130**, 104506; doi:10.1063/1.3078381.
28. Spohr H.V., Patey G.N., *J. Chem. Phys.*, 2010, **132**, 154504; doi:10.1063/1.3380830.
29. Spohr H.V., Patey G.N., *J. Chem. Phys.*, 2010, **132**, 234510; doi:10.1063/1.3430561.
30. Rebelo L.P.N., Canongia Lopes J.N., Esperança J.M.S.S., Filipe E., *J. Phys. Chem. B*, 2005, **109**, 6040; doi:10.1021/jp050430h.
31. Martín-Betancourt M., Romero-Enrique J.M., Rull L.F., *J. Phys. Chem. B*, 2009, **113**, 9046; doi:10.1021/jp903709k.
32. Schröder W., Vale V.R., *J. Phys.: Condens. Matter*, 2009, **21**, 424119; doi:10.1088/0953-8984/21/42/424119.
33. Kalyuzhnyi Y.V., Kahl G., Cummings P.T., *J. Chem. Phys.*, 2004, **120**, 10133; doi:10.1063/1.1737291.
34. Kalyuzhnyi Y.V., Kahl G., Cummings P.T., *J. Chem. Phys.*, 2005, **123**, 124501; doi:10.1063/1.2042347.
35. Boublik T., Nezbeda I., *Chem. Phys. Lett.*, 1977, **46**, 315; doi:10.1016/0009-2614(77)85269-X.
36. Allen M.P., Tildesley D.J., *Computer Simulation of Liquids*. Clarendon Press, Oxford, 1987.
37. Ganzenmüller G., Camp P.J., *J. Chem. Phys.*, 2007, **127**, 154504; doi:10.1063/1.2794042.

38. Kalyuzhnyi Y.V., Protsykevych I.A., Ganzenmüller G., Camp P.J., Europhys. Lett., 2008, **84**, 26001; doi:10.1209/0295-5075/84/26001.
39. Luijten E., Fisher M.E., Panagiotopoulos A.Z., Phys. Rev. Lett., 2002, **88**, 185701; doi:10.1103/PhysRevLett.88.185701.
40. Fisher M.E., J. Phys.: Condens. Matter, 1996, **8**, 9103; doi:10.1088/0953-8984/8/47/002.
41. Plimpton S.J., J. Comp. Phys., 1995, **117**, 1; doi:10.1006/jcph.1995.1039.
42. <http://lammmps.sandia.gov>
43. Hansen J.P., McDonald I.R., Theory of Simple Liquids. 3rd edn., Academic Press, London, 2006.
44. Eyring H., J. Chem. Phys., 1936, **4**, 283; doi:10.1063/1.1749836.
45. Hansen J.P., McDonald I.R., Phys. Rev. A, 1975, **11**, 2111; doi:10.1103/PhysRevA.11.2111.
46. Svishchev I.M., Kusalik P.G., Phys. Chem. Liq., 1994, **26**, 237; doi:10.1080/00319109408029496.
47. Petravic J., Delhomelle J., J. Chem. Phys., 2003, **119**, 8511; doi:10.1063/1.1613256.
48. Kobrak M.N., Sandalow N. – In: Molten Salts. Vol. XIV, 417–425, eds. Mantz R.A., Trulove P.C., De Long H.C., Stafford G.R., Hagiwara M., Costa D.A., The Electrochemical Society, Pennington, New Jersey.
49. Peter C., Kremer K., Faraday Discuss., 2010, **144**, 9; doi:10.1039/B919800H.
50. Hijón C., Español P., Vanden-Eijnden E., Delgado-Buscalioni R., Faraday Discuss., 2010, **144**, 301; doi:10.1039/B902479B.

Фазова поведінка та динаміка в примітивних моделях молекулярно-іонних рідин

Г.С. Ганзенмюллер¹, Ф.Дж. Кемп²

¹ Інститут динаміки швидкотривалих процесів товариства Фраунгофера (Інститут Ернста Маха), Фрайбург, Німеччина

² Школа хімії, Університет Едінбурга, Едінбург, Великобританія

Досліджено фазову поведінку і динаміку молекулярно-іонних рідин з допомогою примітивних моделей та масштабних комп'ютерних моделювань. Використані моделі враховують різницю в розмірах катіона та аніона, положення заряду на катіонах і анізотропію форми катіона, що є визначальними властивостями іонних рідин при кімнатних температурах. Високоточне моделювання методом Монте-Карло використано для побудови фазових діаграм рідина-газ, які в подальшому використовуються для вивчення динаміки іонних рідин. За допомогою моделювання молекулярною динамікою досліджено структуру, трансляційні та обертальні автокореляційні функції, катіонні орієнтаційні автокореляції, самодифузію, в'язкість та частотну залежність провідності. Отримані результати виявляють низку молекулярних механізмів переносу зарядів, включаючи молекулярну трансляцію, обертання та асоціацію.

Ключові слова: іонні рідини, перехід рідина-газ, динаміка, комп'ютерне моделювання
